A Large-Eddy-Simulation Model for the Study of Planetary Boundary-Layer Turbulence

CHIN-HOH MOENG

National Center for Atmospheric Research,[1] Boulder, CO 80307

(Manuscript received 30 January 1984, in final form 4 May 1984)

ABSTRACT

A large-eddy-simulation (LES) model explicitly calculates the large-eddy field and parameterizes the small eddies. The large eddies in the atmospheric boundary layer are believed to be much more important and more flow-dependent than the small eddies. The LES model results are therefore believed to be relatively insensitive to the parameterization scheme for the small eddies.

Deardorff first applied this type of numerical model to boundary-layer turbulence. In order to continue his important work, and to take advantage of the fast Fourier transformation algorithm, a new LES model code which uses a mixed pseudospectral finite-difference method was developed. This LES model is described here and tested with a simple vortex flow and with the Wangara day-33 data.

This model will be used to systematically investigate fundamental problems in the area of boundary-layer turbulence. It is hoped that three-dimensional simulations will give useful statistical information about turbulence structure and improve the closure assumptions in ensemble-mean turbulence modeling.

1. Introduction

Because of the complex physical processes involved in the planetary boundary layer (PBL), it is probably impossible to develop theoretically a general and yet simple ensemble-mean turbulence model for climate and mesoscale applications. Observational and numerical studies have found deficiencies in first-order (K-closure) models, second-order down-gradient diffusion closure models (Wyngaard, 1973; Zeman and Lumley, 1976), and even third-order quasi-normal approximation closure models (Deardorff, 1978; Moeng and Randall, 1984). Uncertainties in the length scale and the closure constants are also serious problems.

To develop empirically such an ensemble-mean turbulence model requires an enormous amount of data concerning the PBL turbulence field under different large-scale conditions. Observational data for the PBL are sometimes difficult to obtain (e.g., in the oceanic stratus-topped PBL). For data to be statistically meaningful, they have to be collected over a large area, but with very fine resolution because of the wide range of sizes of turbulent eddies. Recently, some researchers have attempted to use Doppler radars for such measurements (D. K. Lilly and T. Gal-Chen, personal communication, 1983). Another way of obtaining "data" is by direct numerical calculation of the important part of the flow field from the Navier–Stokes equations, i.e., through large-eddy simulations.

Within the PBL there are different scales of turbulent eddies; large eddies (from ~100 to 1000 m or more) are produced directly by the instability of the mean flow (e.g., shear or buoyancy effects) and small eddies (from a few centimeters to 100 m) by the energy-cascade process from the larger eddies. After many cascade processes, the eddies can be so small that they are believed not to be related to the flow geometry or the source of energy production. At this scale viscous forces dominate and so the effect of the small eddies is mostly to dissipate the turbulent energy rather than to transfer momentum and heat.

A model which explicitly simulates the large eddies but parameterizes the small eddies is called a large-eddy-simulation (LES) model. For three-dimensional turbulence this type of model must be time-dependent and should have a grid size which falls within the inertial subrange. This approach has been applied to meteorological flows by Deardorff (1972) and Sommeria (1976); and to laboratory or engineering flows by the Stanford group (Reynolds, 1981), the Queen Mary College group (Love and Leslie, 1977; Antonopoulos-Domis, 1981), and a German group (Grötzbach and Schumann, 1979). It is discussed and reviewed by Herring (1979) and Ferziger and Leslie (1979).

The first application of the LES approach was made by Deardorff; his model remained for some years the only one applying to PBL turbulence. Using his model, Deardorff obtained many useful insights into PBL turbulence structure, such as the scaling parameters for the convective PBL (Deardorff, 1972). Many questions, however, still remain to be answered. The difficulty of obtaining the detailed structure of turbulent flow through observations, the deficiency of existing ensemble-mean closure models, and the rapid development of large computers are reasons for the further development of LES models to generate

[1] The National Center for Atmospheric Research is sponsored by the National Science Foundation.

"model data" and improve boundary-layer parameterizations.

To continue and extend Deardorff's work, and to take advantage of modern computer techniques in solving the fast Fourier transformation (FFT) algorithm, I have developed a new LES model code. This new model uses a pseudospectral representation in the horizontal directions in which the PBL turbulence is nearly homogeneous, and finite-differencing in the vertical direction. With the same number of grid points, the Fourier representation has better numerical resolution than finite differences (Orszag, 1971a). Other advantages of the Fourier expansion method are that the pressure fluctuation calculation is simple, it is free of phase error, and the filtering procedure for the Leonard stress (Leonard, 1974) can be performed easily.

In this paper, the new model is described and some simulation results are presented. The governing equations for the resolved-scale field are given in Section 2, the subgrid representation is discussed in Section 3, the numerical scheme is described in Section 4, and the boundary conditions are given in Section 5. In Section 6, the accuracy of the numerical scheme is tested through nonlinear simulations of the three-dimensional Taylor–Green vortex problem. The model is then applied to convective PBL flows (Wangara day 33) in Section 7. Section 8 is a summary.

2. Governing equations for the resolved-scale field

To define the resolved variable $\bar{\mathcal{F}}$, Leonard's (1974) filter,

$$\bar{\mathcal{F}}(\mathbf{x}) = \int_D G(\mathbf{x} - \mathbf{x}')\mathcal{F}(\mathbf{x}')d\mathbf{x}' \tag{1}$$

is used, where the integration is over the whole flow domain D. The filtering function $G(\mathbf{x} - \mathbf{x}')$ is a normalized weighting function to be defined later. The overbar denotes the resolved-scale (or large-eddy) field. The effect of this filtering operation is to remove the subgrid-scale fluctuations (or small eddies; $\mathcal{F}'$) from the total field.

Applying the filtering operator to the incompressible Navier–Stokes equations and making the substitution $\mathcal{F}(\mathbf{x}) = \bar{\mathcal{F}}(\mathbf{x}) + \mathcal{F}'(\mathbf{x})$ into the nonlinear advection terms, gives the equations of motion for resolved-scale velocity components $\bar{u}$, $\bar{v}$, $\bar{w}$:

$$\frac{\partial \bar{u}}{\partial t} = \overline{\bar{v}\bar{\zeta}_z} - \overline{\bar{w}\bar{\zeta}_y} + f\bar{v} - \frac{\partial P^*}{\partial x} - \frac{\partial \langle \bar{p} \rangle}{\partial x} - \frac{\partial \tau_{xx}}{\partial x} - \frac{\partial \tau_{xy}}{\partial y} - \frac{\partial \tau_{xz}}{\partial z}, \tag{2}$$

$$\frac{\partial \bar{v}}{\partial t} = \overline{\bar{w}\bar{\zeta}_x} - \overline{\bar{u}\bar{\zeta}_z} - f\bar{u} - \frac{\partial P^*}{\partial y} - \frac{\partial \langle \bar{p} \rangle}{\partial y} - \frac{\partial \tau_{xy}}{\partial x} - \frac{\partial \tau_{yy}}{\partial y} - \frac{\partial \tau_{yz}}{\partial z}, \tag{3}$$

$$\frac{\partial \bar{w}}{\partial t} = \overline{\bar{u}\bar{\zeta}_y} - \overline{\bar{v}\bar{\zeta}_x} + \frac{g\bar{\theta}}{\theta_0} - \frac{\partial P^*}{\partial z} - \frac{\partial \tau_{xz}}{\partial x} - \frac{\partial \tau_{yz}}{\partial y} - \frac{\partial \tau_{zz}}{\partial z} - \left\langle \overline{\bar{u}\bar{\zeta}_y} - \overline{\bar{v}\bar{\zeta}_x} + \frac{g\bar{\theta}}{\theta_0} - \frac{\partial P^*}{\partial z} - \frac{\partial \tau_{xz}}{\partial x} - \frac{\partial \tau_{yz}}{\partial y} - \frac{\partial \tau_{zz}}{\partial z} \right\rangle. \tag{4}$$

Here the angular brackets denote horizontal means; f is the Coriolis parameter, $\bar{\theta}$ the virtual potential temperature, g the gravitational acceleration, ζ_x, ζ_y and ζ_z the vorticity components in x, y and z, and the τ are the subgrid-scale (SGS) Reynolds stresses defined as

$$\tau_{ij} = R_{ij} - R_{kk}\delta_{ij}/3, \tag{5}$$

where

$$R_{ij} = \overline{u_i'u_j'} + \overline{u_i'\bar{u}_j} + \overline{\bar{u}_i u_j'}, \tag{6}$$

$$P^* = \frac{\bar{p}}{\rho_0} + \frac{R_{kk}}{3} + \frac{(\bar{u}_k\bar{u}_k)}{2}. \tag{7}$$

The horizontal-mean pressure gradient force term [the fifth term on the right-hand side of (2) and (3)] is written separately so that it can be treated as an external forcing, i.e., the geostrophic winds in the PBL simulations are prescribed. The nonlinear advection terms are written in rotation form, i.e., the sum of the cross product of velocity and vorticity and the gradient of kinetic energy, in order to conserve the volume-averaged kinetic energy. Equation (4) is solved for the part of the vertical velocity field that deviates from the hydrostatic balance and the horizontal mean, so that $\partial\langle\bar{w}\rangle/\partial t = \langle\bar{w}\rangle = 0$ at all levels.

The continuity equation becomes

$$\frac{\partial \bar{u}}{\partial x} + \frac{\partial \bar{v}}{\partial y} + \frac{\partial \bar{w}}{\partial z} = 0. \tag{8}$$

The pressure field $\bar{p}$ (the deviation from the horizontal mean) is solved by taking the divergence of the equations of motion, using (8), and forming a Poisson equation

$$\nabla^2 P^* = \frac{\partial H_x}{\partial x} + \frac{\partial H_y}{\partial y} + \frac{\partial H_z}{\partial z}, \tag{9}$$

where H_x, H_y and H_z are the sums of the right-hand sides (except the p^* gradient terms) in (2), (3) and (4).

The equation for a filtered conserved thermodynamic variable, e.g., virtual potential temperature $\bar{\theta}$, is

$$\frac{\partial \bar{\theta}}{\partial t} = -\bar{u}\frac{\partial \bar{\theta}}{\partial x} - \bar{v}\frac{\partial \bar{\theta}}{\partial y} - \bar{w}\frac{\partial \bar{\theta}}{\partial z} - \frac{\partial \tau_{\theta x}}{\partial x} - \frac{\partial \tau_{\theta y}}{\partial y} - \frac{\partial \tau_{\theta z}}{\partial z}, \tag{10}$$

where τ_θ are the subgrid turbulence fluxes of virtual potential temperature.

The resolved-scale variables thus defined are continuous in space. One of the choices of filter in (1) is the top-hat function $G = 1/\Delta^3$ within a grid volume Δ^3 and zero outside, as used by Lilly (1967) and Deardorff (1970). Those who use the Fourier trans-

formation approach (e.g., the Stanford group), however, prefer to use the Gaussian function

$$G(\mathbf{x}-\mathbf{x}') = \left(\frac{\sqrt{\gamma/\pi}}{\Delta}\right)^n \exp[-(\sqrt{\gamma}/\Delta)^n(\mathbf{x}-\mathbf{x}')^2], \quad (11)$$

where γ is a constant, Δ the filter width and n the number of dimensions to be filtered. Here the Gaussian filter is applied only in the horizontal directions (i.e., $n = 2$) and the finite-differencing in the vertical direction implicitly supplies top-hat filtering. Following Kwak *et al.* (1975), $\gamma = 6$ and $\Delta = 2\Delta x$, where Δx is the grid spacing in x and y.

3. Subgrid-scale parameterization

The filtered equations discussed above can be solved once the SGS fluxes are determined in terms of the resolved-scale field. In the LES model, the SGS turbulence is a local and instantaneous field; the parameterization problem it presents is quite different from that in ensemble-averaged turbulence models, where the parameterizations cover all scales of eddies. Current SGS turbulence models use empirical constants derived from the statistical properties of turbulence, which do not necessarily hold for the transient and random SGS field. Despite this, however, the small eddies contribute much less heat and momentum transport than the large eddies; they are less flow-dependent and more isotropic; the energy contained within them is weaker. Overall, therefore, the LES model is less sensitive to the parameterization scheme, which parameterizes only the small eddies.

The most widely used SGS model is Smagorinsky's (1963) nonlinear eddy viscosity model, which is derived approximately from the hypothesized balance between shear production and dissipation with the Kolmogorov spectrum (Lilly, 1966). Deardorff (1973) has shown that this approach tends to smear the inversion base which typically overlies the PBL. Moreover, I am mainly interested in buoyancy-driven and transitional PBL flows; for these, a balance between shear production and dissipation rarely exists.

The turbulence energy model used by Deardorff (1980) is adopted here; a prognostic equation is solved for the SGS turbulence energy $\bar{e}'$ (where $\bar{e} = R_{kk}/2$):

$$\frac{\partial \bar{e}'}{\partial t} = -\bar{u}_i\frac{\partial \bar{e}'}{\partial x_i} - \overline{u_i'u_j'}\frac{\partial \bar{u}_i}{\partial x_j} + \frac{g}{\theta_0}\overline{w'\theta'} - \frac{\partial[\overline{u_i'(e'+p'/\rho_0)}]}{\partial x_i} - \epsilon, \quad (12)$$

where ϵ is the dissipation rate. The SGS fluxes are related to the resolved-scale field as

$$\tau_{ij} = -K_M\left(\frac{\partial \bar{u}_i}{\partial x_j} + \frac{\partial \bar{u}_j}{\partial x_i}\right), \quad (13)$$

$$\tau_{\theta i} = -K_H\frac{\partial \bar{\theta}}{\partial x_i}, \quad (14)$$

where K_M and K_H are the SGS eddy coefficients for momentum and heat.

The energy cascade due to the Leonard stress $(\bar{\bar{u}}_i\bar{\bar{u}}_j - \bar{u}_i\bar{u}_j)$ is included in the resolvable-scale advection term, through the double-filtering procedure. However, in deriving the SGS energy equation (12), I have neglected the Leonard stress and $u_i'\bar{u}_j$ terms, since assumptions to be made later for the last two terms in (12) are probably more critical.

The closure assumptions made here in order to solve (12) are the downgradient diffusion assumption

$$\overline{u_i'(e'+p'/\rho_0)} = -2K_M\frac{\partial \bar{e}'}{\partial x_i} \quad (15)$$

and the Kolmogoroff hypothesis

$$\epsilon = \frac{C\bar{e}'^{3/2}}{l}, \quad (16)$$

with

$$C = 0.19 + (0.51l/\Delta s). \quad (17)$$

The value of C is adjusted to 3.9 at the lowest level due to wall effects suggested by Deardorff (1980).

The length scale l is

$$l = \Delta s = (\Delta x\Delta y\Delta z)^{1/3} \quad (18a)$$

when the stratification is negative and

$$l = l_s = 0.76\bar{e}'^{1/2}\left(\frac{g}{\theta_0}\frac{\partial \bar{\theta}}{\partial z}\right)^{-1/2} \quad (18b)$$

when the stratification is positive and $l_s < \Delta s$. This modification was suggested by Deardorff to take into account the possible small mixing length in a stably stratified region.

The eddy coefficients are proportional to the product of the length scale and the velocity scale $(\bar{e}')^{1/2}$:

$$K_M = 0.1l\bar{e}'^{1/2}, \quad (19)$$

$$K_H = [1 + (2l/\Delta s)]K_M. \quad (20)$$

The constants in (15), (17), (18b), (19) and (20) are entirely empirical (Deardorff, 1973, 1980). However, the SGS parameterization scheme should not affect the model result too much since it treats only the small eddies.

4. Numerical scheme

The statistical properties of PBL turbulence are nearly horizontally homogeneous when the external forcing is uniform. Hence periodic boundary conditions can be applied in both the x and y directions. In the vertical, however, the turbulence energy sources and sinks are not uniformly distributed—the buoyancy source in a convective clear PBL is mainly at the surface, while the buoyancy sink is in the interfacial entraining layer near the PBL top.

A mixed scheme of Fourier expansion in the horizontal directions and finite differencing in the

vertical is therefore appropriate for the numerical simulation of PBL turbulence. This technique has been employed by the Stanford group (e.g., Moin *et al.*, 1978) in simulating engineering flows, and by spectral general circulation modelers.

The pseudospectral method (Fox and Orszag, 1973) is chosen to evaluate the horizontal derivatives. To calculate the x-derivatives of $\bar{u}$, for example, the variable $\bar{u}$ is first transformed into the Fourier space in x:

$$\hat{\bar{u}}(k_m, y, z) = \frac{1}{N}\sum_{n=1}^{N} \bar{u}(x_n, y, z)\exp(-ik_m x_n); \quad (21)$$

then the transform coefficient $\hat{\bar{u}}$ is multiplied by ik_m, and $ik_m\hat{\bar{u}}$ is inversely transformed back to the grid points using

$$\left(\frac{\partial \bar{u}}{\partial x}\right)_n = \sum_{m=-(N/2)+1}^{N/2} ik_m\hat{\bar{u}}(k_m, y, z)\exp(ik_m x_n), \quad (22)$$

where N is the number of grid points in this direction, carets denote Fourier-transformed quantities, and $k_m = 2\pi m/N\Delta x$ is the wavenumber. The maximum wavenumber of the resolved scale $m = N/2$ corresponds to 2Δ waves, which are truncated in this model.

Centered finite-differences of second-order accuracy are used to evaluate the vertical derivatives.

The nonlinear advection terms in (2), (3) and (4) are written in neither advective nor flux form, but in two terms: The cross product of velocity and vorticity and the gradient of kinetic energy. In this way, the conservation property of the volume-mean kinetic energy can be readily satisfied by the use of only integration by parts and the continuity equation. The identity

$$u_i\left(\frac{\partial u_i}{\partial x_j}\right) = \frac{\partial[(u_i u_i)/2]}{\partial x_j}, \quad (23)$$

which does not hold with pseudospectral differencing, is not required here (Mansour *et al.*, 1979). Once the total energy is bounded, the aliasing error, though it exists, cannot grow exponentially and the nonlinear instability is controlled (Arakawa, 1966).

The nonlinear advection term in the scalar equation (10), however, can only be written in advective or flux form. To make it conserve the integral of $\bar{\theta}^2$, as it does in the continuous form, one-half of the advective form and one-half of the flux form are used. Because

$$\int u\theta\frac{\partial\theta}{\partial x}\,dV + \int \theta\frac{\partial(u\theta)}{\partial x}\,dV = 0 \quad (24)$$

over a closed domain, the conservation property in discrete form can be easily satisfied. The same scheme is applied to (12). Care should be taken in using this scheme; $\nabla\cdot\mathbf{V} = 0$ is implicitly used and must therefore be satisfied at all times, even at the initial stage.

Notice that the aliasing error exists in full strength since the nonlinear multiplication is made in physical grid space. No smoothing or truncation operators are applied in this model, except that the horizontal 2Δ waves are truncated. To examine the significance of the aliasing error, I have tested the model with a PBL simulation in which the top one-third of the admissible wave numbers ($k > \frac{2}{3}K_{\max}$) are eliminated so that none of the aliasing error exists (Orszag, 1971b). No significant difference in results, with and without the aliasing error, was observed. The insensitivity to the existence of the aliasing error is also observed in a simulation of the Taylor–Green vortex flow (Section 6).

By using Fourier transformations in x and y, the filtering process can be accomplished through the convolution theorem; for example, to calculate $\bar{u}\bar{\xi}_y$, the convolution relationship

$$\widehat{(\bar{u}\bar{\xi}_y)} = (L^2)\hat{G}\widehat{(\bar{u}\bar{\xi}_y)} \quad (25)$$

is applied, where L is the size of the numerical domain in both x and y, and $\hat{G}$ is the Fourier transformation of the function given in (11) and an inverse Fourier transformation is carried out.

The time advancement is solved using the Adams–Bashforth scheme. In the PBL experiments I used a 3 s time interval, with a total of $32 \times 32 \times 40$ grid points covering a numerical domain of $5 \times 5 \times 2$ km. A staggered spacing is used in z so that $\bar{w}$ is located at the intermediate levels, between which $\bar{u}$, $\bar{v}$, $\bar{\theta}$, $\bar{p}$ and $\bar{e}'$ are defined. Nonstaggered spacing is used in x and y. The lowest level for $\bar{w}$ is the surface, and that for $\bar{u}$, $\bar{v}$, $\bar{\theta}$, $\bar{p}$ and $\bar{e}'$ is $z = \Delta z/2$. Subgrid-scale fluxes are located such that their vertical derivatives are at the level of the mean variables they are to modify (e.g., τ_{xx} at the u-level and τ_{xz} at the w-level).

To ensure incompressibility, the Poisson equation is solved by applying the numerical divergence operator $\delta/\delta x_i$ to the numerical form of the equations of motion:

$$\frac{\delta^2 P^*}{\delta x_i^2} = \frac{\delta H_x}{\delta x} + \frac{\delta H_y}{\delta y} + \frac{\delta H_z}{\delta z} + \frac{2}{3}\frac{(\delta u_i/\delta x_i)}{\Delta t}, \quad (26)$$

where H_x, H_y and H_z are the exact numerical forms of the right-hand-side functions, except the P^* gradient term, in (2), (3) and (4). At time step n, H are used to calculate P^* at time step n. A small correction of the divergence field at time step n, shown as the last term in (26), is added to avoid the accumulation of any nonzero divergence owing to truncation errors or divergence in the initial field (Deardorff, 1973). After making the Fourier transformation in x and y, and the centered finite-difference in z, a tridiagonal matrix is then solved for P^*. Because a vertically staggered grid is used, the second derivatives in z are calculated over a two-grid interval instead of four, as it would be if a nonstaggered grid were used.

5. Boundary conditions

If no SGS effects are included, the flow is inviscid and the condition $\bar{w}_0 = 0$ at the surface is sufficient for the wall boundary. If SGS effects are included, the vertical gradient of the velocity at $z_1 = 25$ m is required to compute the shear production term in (12). From the similarity formula, e.g., for the u-component,

$$\left(\frac{\partial \bar{u}}{\partial z}\right) = \frac{u^* \cos\phi}{\kappa(\frac{1}{2}z_1)} \Phi\left(\frac{\frac{1}{2}z_1}{L}\right) \quad \text{at} \quad z = \tfrac{1}{2}z_1, \tag{27}$$

the vertical gradient of $\bar{u}$ at $z = 12.5$ m is computed. Here $\Phi(z_1/L) = [1 - (15z_1/L)]^{-1/4}$ if the horizontal-mean surface heat flux is positive, and $\Phi(z_1/L) = 1 + (4.7z_1/L)$ if it is negative; u^* is the local friction velocity, defined as $(\tau_{xz}^2 + \tau_{yz}^2)^{1/4}$, and ϕ is the angle of surface stress away from the x-direction. The gradient at $z_1 = 25$ m is then obtained by interpolating those at 50 and 12.5 m.

The SGS vertical fluxes at the surface, derived from $\tau = C_D S_1 \bar{V}_1$ and using $S_1 = \langle S_1 \rangle + S_1''$ (see Appendix; J. C. Wyngaard, personal communication, 1983), etc., are

$$(\tau_{xz})_0 = \langle \tau_{xz} \rangle_0 \frac{S_1 \langle \bar{u}_1 \rangle + \langle S_1 \rangle (\bar{u}_1 - \langle \bar{u}_1 \rangle)}{\langle S_1 \rangle \langle \bar{u}_1 \rangle}, \tag{28}$$

$$(\tau_{yz})_0 = \langle \tau_{yz} \rangle_0 \frac{S_1 \langle \bar{v}_1 \rangle + \langle S_1 \rangle (\bar{v}_1 - \langle \bar{v}_1 \rangle)}{\langle S_1 \rangle \langle v_1 \rangle}, \tag{29}$$

$$(\tau_{\theta z})_0 = \langle \tau_{\theta z} \rangle_0 \frac{S_1 (\langle \bar{\theta}_1 \rangle - \theta_0) + \langle S_1 \rangle (\bar{\theta}_1 - \langle \bar{\theta}_1 \rangle)}{\langle S_1 \rangle \langle \langle \bar{\theta}_1 \rangle - \theta_0 \rangle}, \tag{30}$$

where $S_1 = (\bar{u}_1^2 + \bar{v}_1^2)^{1/2}$ is the wind speed, subscript 1 denotes the value at $z = 25$ m, subscript zero the value at the surface, and the double prime the deviation from the horizontal mean. The formulas used by Schumann *et al.* (1980) can be derived from (28), (29) and (30) by neglecting the local fluctuation of the wind speed; i.e., letting $S_1 = \langle S_1 \rangle$.

Close to the surface, only very weak large eddies exist in w, and hence it can be assumed that the SGS eddies are entirely responsible for transferring heat and momentum vertically. With this boundary condition, the horizontal-mean SGS surface fluxes, as well as the local SGS fluxes, are then in accordance with the similarity property. Using (28)–(30), the similarity formula is calculated only for the horizontal mean. In this study the horizontal-mean surface fluxes are prescribed. However, they can be calculated from the Monin–Obukhov similarity using the empirical formula proposed by Businger *et al.* (1971). This procedure was bypassed for this preliminary study.

The top boundary conditions are zero vertical velocity ($\bar{w} = 0$), zero SGS turbulence fields, and $\partial \bar{u}/\partial z = 0$, $\partial \bar{v}/\partial z = 0$, and $\partial \bar{\theta}/\partial z =$ constant across the $\bar{w} = 0$ level. Admittedly, these upper boundary conditions do not allow transmission of gravity waves, which can be generated in the stably stratified layer. Use of a radiative upper boundary condition (e.g., Klemp and Durran, 1983) would be more favorable.

The tridiagonal system for the P^* field in (26) is computed with Neumann boundary conditions derived from (4) ($\bar{w} = 0$ at both the top and bottom boundaries), with two levels added above and below the horizontal boundaries.

6. A check of model accuracy

The accuracy of the basic dynamic framework of this model was checked by directly simulating the three-dimensional Taylor and Green (1937) vortex flow; it is the simplest nonlinear three-dimensional incompressible flow for checking the numerical scheme. The SGS parameterization and filtering process are turned off. Molecular dissipation terms (e.g., $\nu\nabla^2\bar{u}$ in the u-equation) with kinematic viscosity $\nu = 1/\mathrm{Re}$, where Re is the Reynolds number, are added into (2), (3) and (4). The nonlinear advection terms induce vortex stretching and tilting which increase the mean-square vorticity and cause the kinetic energy cascade from the larger to smaller scales. The molecular dissipation terms reduce both mean-square vorticity and kinetic energy. Because of the energy-cascading, the aliasing effect in the model can be studied.

The initial conditions are

$$\bar{u}(x, y, z) = \cos(x) \sin(y) \cos(z), \tag{31}$$

$$\bar{v}(x, y, z) = -\sin(x) \cos(y) \cos(z), \tag{32}$$

$$\bar{w}(x, y, z) = 0, \tag{33}$$

and Re = 200 is used. Periodic boundary conditions are applied in all x, y and z directions, where these coordinates were made dimensionless for this check.

Two runs, one with a grid number of $16 \times 16 \times 16$ and another with $16 \times 16 \times 32$, are made in a total nondimensional numerical domain of $2\pi \times 2\pi \times 2\pi$. These are equivalent to a cutoff Fourier expansion wavenumber of $k_{\max} = 8$ in the horizontal directions. The time interval is $\Delta x/10u_{\max}$, which is ~ 0.04.

The results were compared to an analytical solution (Taylor and Green, 1937) for a short period of time integration, and to numerical simulations by Orszag (1971a) using an alias-free spectral (Galerkin) model and the Arakawa second-order finite-difference method. Figure 1 shows the time evolution of the mean-square vorticity, which is a measure of the energy cascading rate (or dissipation rate). The mean-square vorticity increases when the nonlinear effect dominates, and decreases when the dissipation effect dominates.

My first simulation, with the coarse grid in all three directions, compares well with the analytical

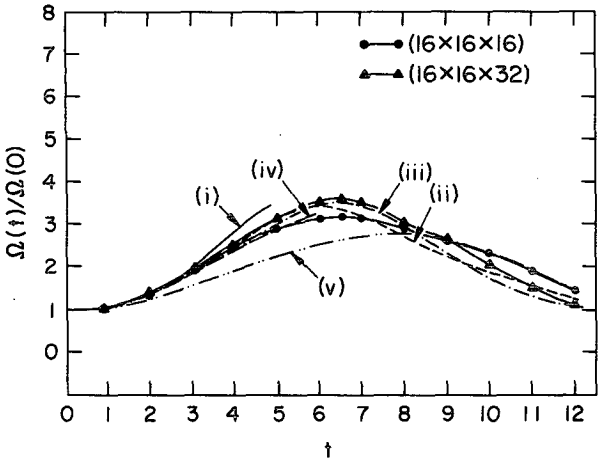

FIG. 1. Mean-square vorticity (nondimensionalized by its initial value) as a function of time (nondimensionalized by the eddy turnover time). Curve (i) is the analytical solution from Taylor and Green (1937); curves (ii) and (iii) are solutions of a Galerkin model with cutoff k = 16 and 8, respectively (Orszag, 1971a); curves (iv) and (v) are solutions of a centered finite-difference model on 32 × 32 × 32 and 16 × 16 × 16 grids, respectively (Orszag, 1971a); curves with triangles and dots are solutions of this mixed pseudospectral finite-difference model on 16 × 16 × 32 and 16 × 16 × 16 grids, respectively.

solution and Orszag's simulations. Here the coarse grid represents N = 16 and the fine grid is N = 32, where N is the grid number along x or y. The finite-difference model with the coarse grid gives a considerably less accurate simulation; judging from this, the model was rerun using the fine grid in the finite-differencing direction (z), and a result closer to that of the fine-grid spectral model was obtained. This mixed pseudospectral finite-difference model, even with aliasing errors, simulates an energy transfer process almost identical to that of an alias-free spectral model.

7. Application to convective PBL flows

The day-33 Wangara data (Clark *et al.*, 1971) from hour 9 to hour 16 were simulated. For a grid number of 32 × 32 × 40, each simulation hour required about one computer hour on the NCAR CRAY-1. The time step was Δt = 3 s.

For simplicity, the moisture field and radiation effects were excluded. The horizontally averaged surface stress and heat flux were given from the observed data. The horizontally-averaged pressure gradient force was obtained from the prescribed x-component geostrophic wind, which was -5.5 m s^{-1} at the surface, linearly increasing to -2.6 m s^{-1} at 1 km and -1.2 m s^{-1} at 2 km. The y-component geostrophic wind was zero. The Coriolis parameter was $f = -0.826 \times 10^{-4}$ s^{-1}. The initial conditions were obtained from the observed horizontally-averaged $\bar{u}$, $\bar{v}$ and $\bar{\theta}$ at hour 9 of day 33, superimposed with very small amplitude random fluctuations to start the resolvable turbulence motions. The dry static energy ($C_pT + gz$) was chosen to be the thermodynamic variable θ.

Figure 2 shows the field structure of the large eddies in an x–z plane at hour 14. At this time the average depth of the PBL was 1150 m. Therefore, the largest thermally induced eddy was on the order of 1 km in both vertical and horizontal extent. The fluctuations in the stable layer above the PBL are internal gravity waves.

The model outputs were averaged over each horizontal plane; the horizontally-averaged fields were considered to be ensemble-mean properties. These statistical properties were then compared with observational data or Deardorff's (1974a,b) results. The field of dry static energy is shown in Fig. 3. At hours 12 and 15, the observed PBL top heights, defined at the inversion base, are at ~1150 and 1250 m.

a. A comparison of results with those of Deardorff (1974a,b)

The vertical velocity variance, nondimensionalized by w_*^2, where w_* is the convective velocity scale, is shown in Fig. 4. The maximum, which occurs at about $z \sim 0.3$–$0.4z_i$, has a value of $\sim 0.42w_*^2$, comparable with Deardorff's (1974a,b) result. At $z = z_i$, $\langle \bar{w}^2 \rangle$ is $\sim 0.08w_*^2$. The horizontal velocity variance (Fig. 5), again nondimensionalized by w_*^2, shows an interesting feature. The two model results do not quite agree with each other; my results show a local maximum at hours 14 and 16 near the PBL top. A linear study by Carruthers and Hunt (1983) shows an increase of ~12.5–25% in the horizontal velocity variances as a homogeneous turbulent flow interfering with a stably stratified layer above. However, what actually causes the difference between the two models is not clear.

The vertical velocity skewness is given in Fig. 6. Observational studies (Wyngaard, 1973) show that this skewness is positive in the surface layer. However, both LES models simulate small negative skewness near the surface; the cause of this failure may be the fact that the skewness there resides in what are the SGS eddies of the model. As pointed out by J. W. Deardorff (personal communication, 1983), it would be interesting to filter the observational data in a manner that simulates the model's filter, before calculating the skewness and comparing it with the model's values.

Even though both predicted maxima of $\langle w^2 \rangle / w_*^2$ (Fig. 4) and $\langle w^3 \rangle / w_*^3$ (not shown) in the middle layer agree with observations, the skewness does not. The skewness measured by Lenschow *et al.* (1980) shows a nearly constant (~0.6) distribution with height, while models clearly simulate maxima at $z/z_i \approx 0.9$. This discrepancy seems due to the model's sharper gradient of the vertical velocity variance near the PBL top.

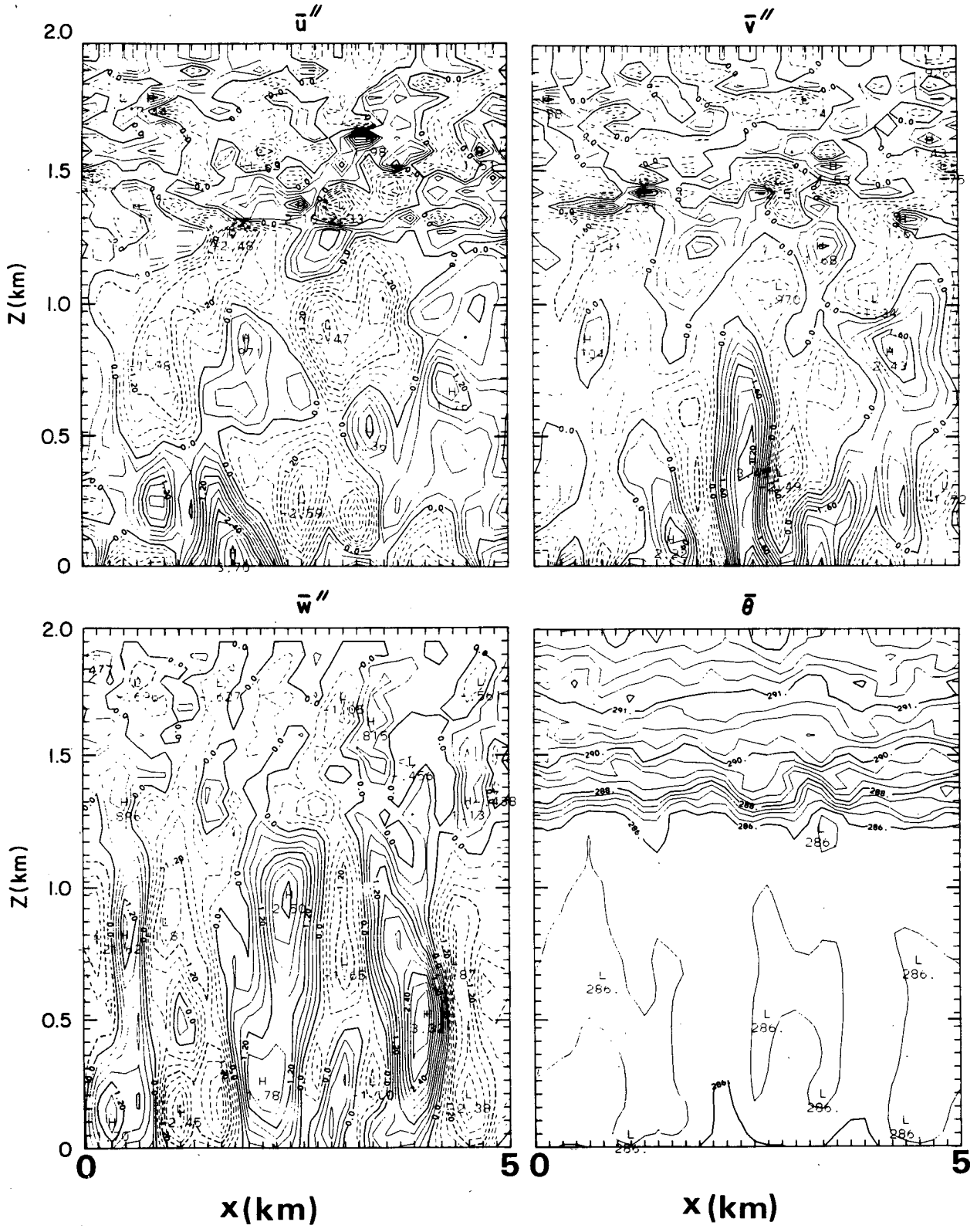

FIG. 2. Contour plots of $\bar{u}''$, $\bar{v}''$, $\bar{w}''$ and $\bar{\theta}$ in a vertical cross section on an x–z plane ($y = 4\Delta y$) at hour 14.

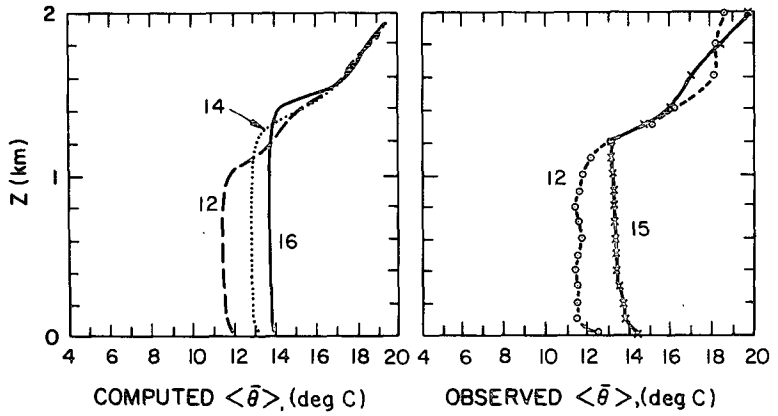

FIG. 3. Vertical profiles of the horizontal mean $\bar{\theta}$; computed at hours 12, 14 and 16, and observed at hours 12 and 15, day 33.

b. A justification of large-eddy-simulation modeling

As stated before, large eddies are believed to transfer most of the momentum and heat and to contain much of the energy; on the other hand, the only major role that the small eddies play (outside of the surface layer) is to dissipate the energy. Figures 7 and 8, which show the turbulent energy and heat flux, respectively, indicate the different properties of the large and small eddies.

The small eddies can indirectly affect the heat transfer by modifying the large eddy field. I therefore analyzed the budgets of resolvable-scale energy and heat flux to study the influence of SGS parameterizations on the model results. The equations of the resolvable-scale energy $K = (\bar{u}''^2 + \bar{v}''^2 + \bar{w}''^2)/2$ and the heat flux are

$$\frac{\partial\langle K\rangle}{\partial t} = \left\langle \left(\overline{\bar{v}\bar{\xi}}_z - \overline{\bar{w}\bar{\xi}}_y - \frac{\partial K}{\partial x}\right)''\bar{u}'' + \left(\overline{\bar{w}\bar{\xi}}_x - \overline{\bar{u}\bar{\xi}}_z - \frac{\partial K}{\partial y}\right)''\bar{v}'' + \left(\overline{\bar{u}\bar{\xi}}_y - \overline{\bar{v}\bar{\xi}}_x - \frac{\partial K}{\partial z}\right)''\bar{w}'' \right\rangle + \frac{g}{\theta_0}\langle\bar{\theta}''\bar{w}''\rangle - \frac{1}{\rho_0}\left\langle \frac{\partial\bar{p}''}{\partial x}\bar{u}'' + \frac{\partial\bar{p}''}{\partial y}\bar{v}'' + \frac{\partial\bar{p}''}{\partial z}\bar{w}'' \right\rangle - \left\langle \left(\nabla\cdot\tau_x + \frac{2}{3}\frac{\partial\bar{e}'}{\partial x}\right)''\bar{u}'' + \left(\nabla\cdot\tau_y + \frac{2}{3}\frac{\partial\bar{e}'}{\partial y}\right)''\bar{v}'' + \left(\nabla\cdot\tau_z + \frac{2}{3}\frac{\partial\bar{e}'}{\partial z}\right)''\bar{w}'' \right\rangle, \quad (34)$$

$$\frac{\partial\langle\bar{w}''\bar{\theta}''\rangle}{\partial t} = \left\langle \left(\overline{\bar{u}\bar{\xi}}_y - \overline{\bar{v}\bar{\xi}}_x - \frac{\partial K}{\partial z}\right)''\bar{\theta}'' - (\bar{\mathbf{v}}\cdot\nabla\bar{\theta})''\bar{w}'' \right\rangle + \frac{g}{\theta_0}\langle\bar{\theta}''^2\rangle - \frac{1}{\rho_0}\left\langle \frac{\partial\bar{p}''}{\partial z}\bar{\theta}'' \right\rangle - \left\langle \left(\nabla\cdot\tau_z + \frac{2}{3}\frac{\partial\bar{e}'}{\partial z}\right)''\bar{\theta}'' + (\nabla\cdot\tau_\theta)''\bar{w}'' \right\rangle, \quad (35)$$

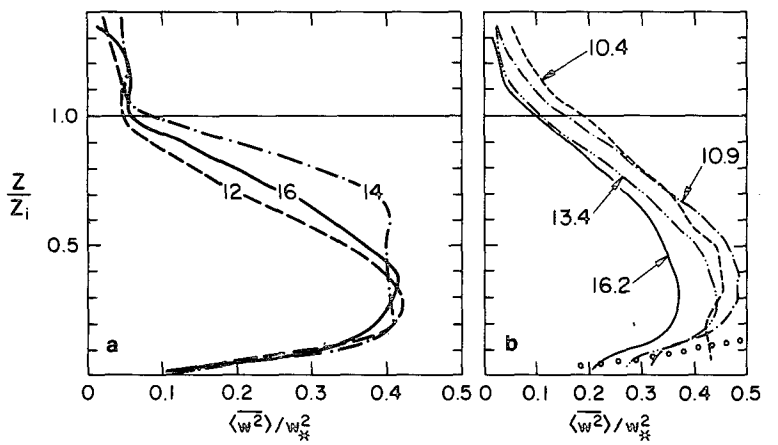

FIG. 4. Vertical profiles of dimensionless vertical velocity variances; (a) from the mixed pseudospectral finite-difference model on a 32 × 32 × 40 grid at hours 12, 14 and 16, and (b) from Deardorff's (1974a,b) finite-difference model on a 40 × 40 × 40 grid at hours 10.4, 10.9, 13.4 and 16.2.

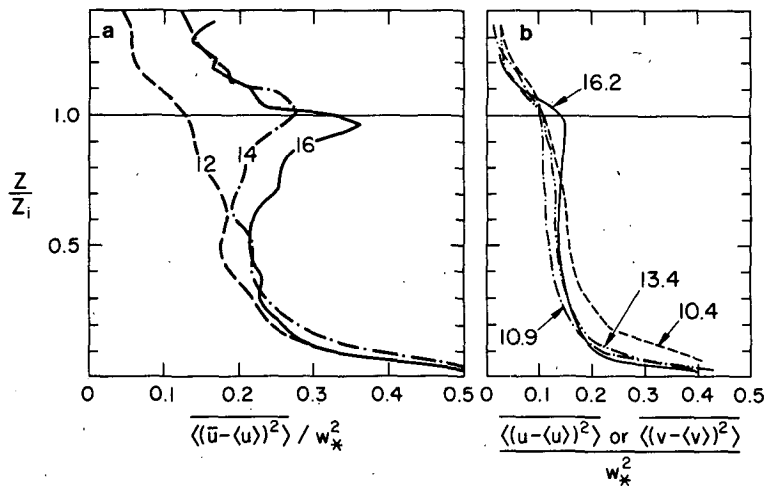

FIG. 5. As in Fig. 4 but for the horizontal velocity variance.

where the first term is the advection effect, the second is the buoyancy effect, the third is the pressure effect, and the fourth is the SGS effect. Again, the double prime denotes the deviation from the horizontal mean, which is represented by angular brackets.

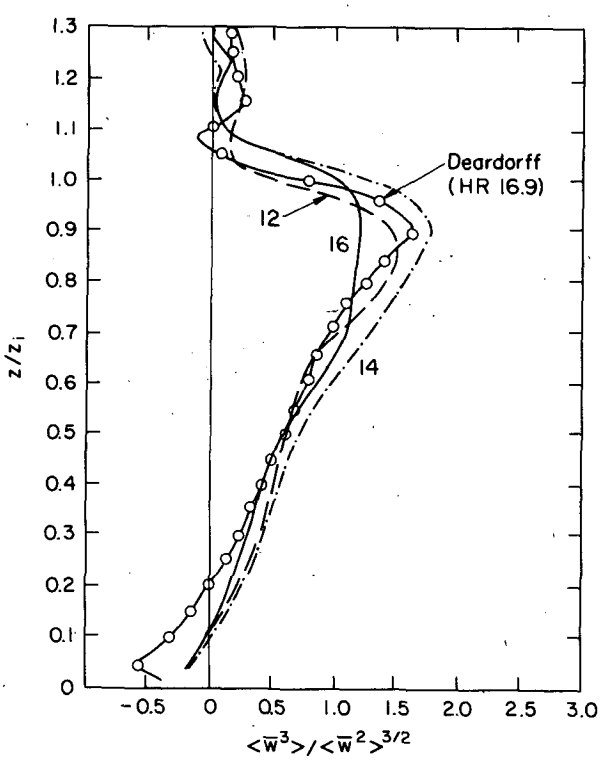

FIG. 6. Vertical profiles of the vertical velocity skewness: The dashed curve is for hour 12, the dashed-dotted curve for hour 14 and the solid curve for hour 16; from the mixed pseudospectral finite-difference model on a 32 × 32 × 40 grid. The curve with dotted circles is from Deardorff's (1974a,b) model on a 40 × 40 × 40 grid for hour 16.9.

The SGS term in Fig. 9 is the amount of energy cascading (excluding the transfer through the Leonard stress), which is ultimately dissipated in the smallest eddies. In the convective PBL, the buoyancy is the main driving force. The advection term, which includes the effects of both the mean wind shear and the nonlinear vertical transport, is negative in the lower layer and positive in the upper layer; it transports energy upward. The pressure effect comes only from the vertical pressure diffusion.

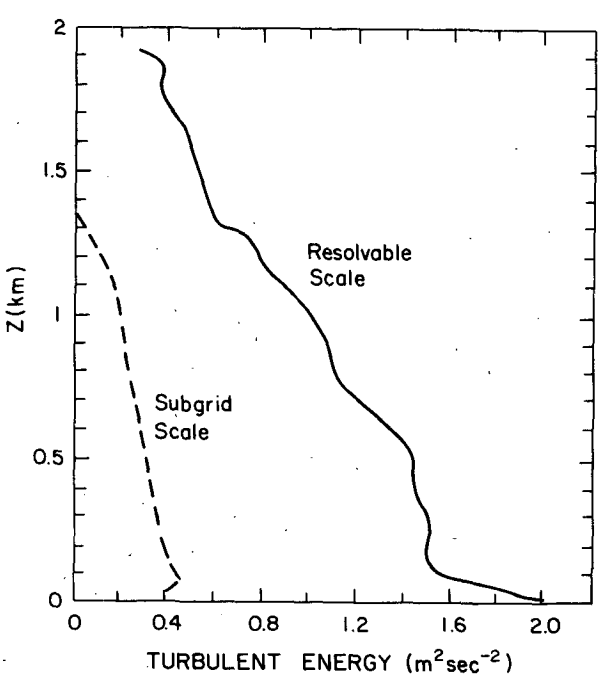

FIG. 7. Vertical profiles of the horizontal mean turbulent energy of the resolvable-scale field (solid curve) and the subgrid-scale field (dashed curve), respectively.

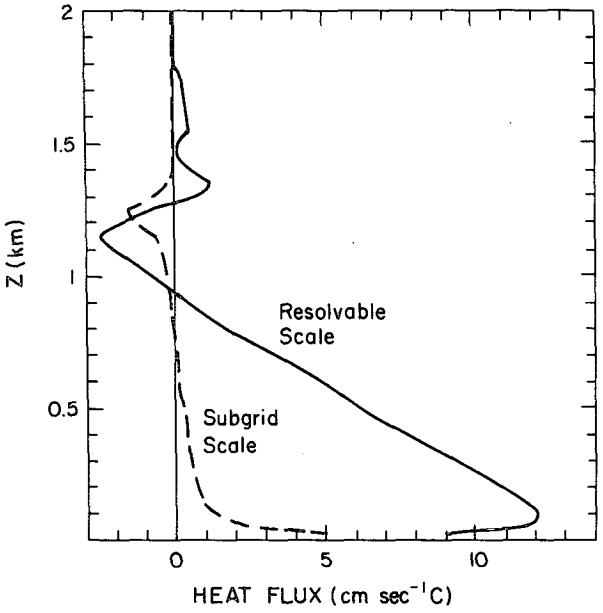

FIG. 8. As in Fig. 7 but for the heat flux.

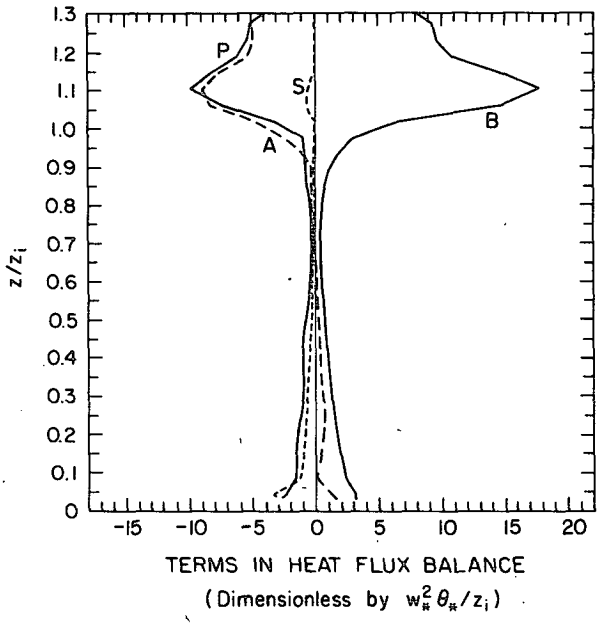

FIG. 10. As in Fig. 9 but for the resolvable-scale heat flux balance.

Figure 10 shows the budgets for the resolvable-scale heat flux and, as expected, the SGS effect is negligibly small except near the surface. The buoyancy effect nearly balances the sum of the advection and pressure effects.

The momentum flux balance is not shown here because of larger sampling errors (Wyngaard, 1973); besides the 5 × 5 km horizontal averaging, some time-averaging is also needed in order to obtain statistically meaningful data.

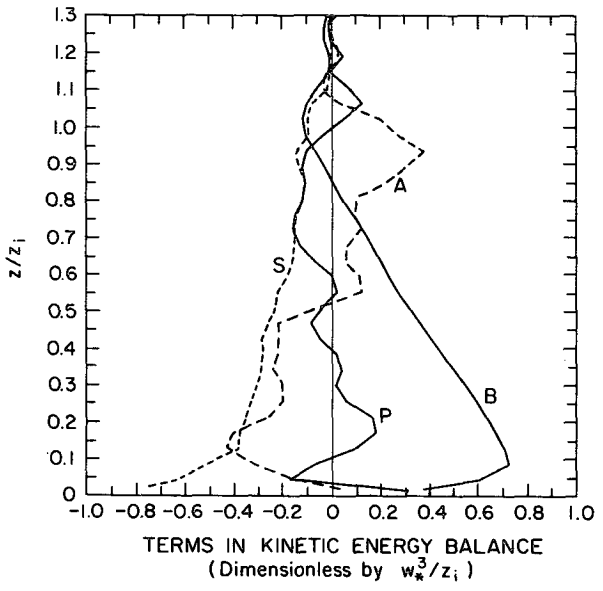

FIG. 9. Vertical profiles of the budget terms in the resolvable-scale turbulent energy balance. Curve B is the buoyancy term, curve P the pressure-related term, curve A the advection term, and curve S the subgrid-scale term.

8. Summary

A large-eddy-simulation (LES) model which uses a mixed pseudospectral and finite-difference scheme has been described. This model is tested successfully on a laboratory vortex flow and a convective PBL flow.

The model output shows that the resolvable-scale eddies contain more turbulent energy and transfer more heat than do the subgrid-scale eddies. The subgrid-scale eddies mainly dissipate the turbulent energy which cascades from the resolvable-scale eddies; they do not contribute much in heat transfer either directly or indirectly, except near the surface.

Through direct simulations of the large-eddy part of turbulent flows, instantaneous, detailed flow structure and statistical properties can be obtained. With the increasing speed of large computers, it is expected that LES models will become useful experimental tools for the study of geophysical turbulence and will provide guidance in developing PBL ensemble-mean closure models.

Acknowledgments. I thank Drs. J. B. Klemp, J. R. Herring and J. C. Wyngaard at NCAR for their helpful assistance and discussions. Thanks also to Drs. J. Deardorff, H. Lin, D. Randall and R. Rotunno for their comments. My sincere appreciation goes to Ms. Hope Hamilton, Ms. Marsha Sime and H. R. Howard for preparing the manuscript.

APPENDIX

Derivation of Eqs. (28)–(30)

Separating the wind field into the horizontal mean and the fluctuation from the mean, $\tau_0 = C_D S_1 \mathbf{V}_1$ becomes

$$\tau_0 = C_D\langle S_1\rangle\langle \mathbf{V}_1\rangle + C_D\langle S_1\rangle \mathbf{V}_1'' + C_D S_1''\langle \mathbf{V}_1\rangle + C_D S_1''\mathbf{V}_1''. \quad \text{(A1)}$$

Taking the horizontal mean of (A1) gives

$$\langle\tau\rangle_0 = C_D\langle S_1\rangle\langle \mathbf{V}_1\rangle + C_D\langle S_1''\mathbf{V}_1''\rangle. \quad \text{(A2)}$$

From (A2), (A1) becomes

$$\tau_0 = C_D\langle S_1\rangle \mathbf{V}_1'' + C_D S_1''\langle \mathbf{V}_1\rangle + \langle\tau\rangle_0 + (C_D S_1''\mathbf{V}_1'' - C_D\langle S_1''\mathbf{V}_1''\rangle) \quad \text{(A3)}$$

and the drag coefficient C_D is given by

$$C_D \approx \frac{\langle\tau\rangle_0}{\langle S_1\rangle\langle \mathbf{V}_1\rangle}. \quad \text{(A4)}$$

Assuming that the two quantities inside the parentheses in (A3) are nearly the same, we have

$$\tau_0 = \langle\tau\rangle_0\left(\frac{S_1\langle \mathbf{V}_1\rangle + \langle S_1\rangle(\mathbf{V}_1 - \langle \mathbf{V}_1\rangle)}{\langle S_1\rangle\langle \mathbf{V}_1\rangle}\right), \quad \text{(A5)}$$

which is a vector expression of (28) and (29). Equation (30) is similarly derived. The drag coefficient in (A4) is constant horizontally; therefore, Eqs. (28)–(30) are appropriate only if the surface stability or the roughness do not vary much horizontally.

REFERENCES

Antonopoulous-Domis, M., 1981: Large-eddy simulation of a passive scalar in isotropic turbulence. *J. Fluid Mech.*, **104,** 55–79.

Arakawa, A., 1966: Computational design for long-term numerical integration of the equations of fluid motion: I. Two-dimensional incompressible flow. *J. Comput. Phys.*, **1,** 119–143.

Businger, J. A., J. C. Wyngaard, Y. Izumi and E. F. Bradley, 1971: Flux-profile relationships in the atmospheric surface layer. *J. Atmos. Sci.*, **28,** 181–189.

Carruthers, D. J., and J. C. R. Hunt, 1983: Velocity fluctuations near an interface between a turbulent region and a stably stratified layer. Submitted to *J. Fluid Mech.*

Clark, R. H., A. J. Dyer, R. R. Brook, D. G. Reid and A. J. Troup, 1971: The Wangara experiment: Boundary layer data. Tech. Pap. No. 19, CSIRO Div. Meteor. Phys., Melbourne, 340 pp.

Deardorff, J. W., 1970: A numerical study of three-dimensional turbulent channel flow at large Reynolds numbers. *J. Fluid Mech.*, **41,** 453–480.

——, 1972: Numerical investigation of neutral and unstable planetary boundary layers. *J. Atmos. Sci.*, **29,** 91–115.

——, 1973: The use of subgrid transport equations in a three-dimensional model of atmospheric turbulence. *J. Fluids Eng.*, **95,** 429–438.

——, 1974a: Three-dimensional numerical study of the height and mean structure of a heated planetary boundary layer. *Bound.-Layer Meteor.*, **7,** 81–106.

——, 1974b: Three-dimensional numerical study of turbulence in an entraining mixed layer. *Bound.-Layer Meteor.*, **7,** 199–226.

——, 1978: Closure of second- and third-moment rate equations for diffusion in homogeneous turbulence. *Phys. Fluids,* **21,** 525–530.

——, 1980: Stratocumulus-capped mixed layers derived from a three-dimensional model. *Bound.-Layer Meteor.*, **18,** 495–527.

Ferziger, J. H., and D. C. Leslie, 1979: Large eddy simulation—A predictive approach to turbulent flow computation. Pap., 79-1441, Amer. Inst. Aeronaut. Astronaut.

Fox, D. G., and S. A. Orszag, 1973: Pseudospectral approximation to two-dimensional turbulence. *J. Comput. Phys.*, **11,** 612–619.

Grötzbach, G., and U. Schumann, 1979: Direct numerical simulation of turbulent velocity, pressure, and temperature fields in channel flows. *Turb. Shear Flows,* **1,** 370–385.

Herring, J. R., 1979: Subgrid scale modeling—An introduction and overview. *Turb. Shear Flows,* **1,** 347–352.

Klemp, J. B., and D. R. Durran, 1983: An upper boundary condition permitting internal gravity wave radiation in numerical mesoscale models. *Mon. Wea. Rev.*, **111,** 430–444.

Kwak, D., W. C. Reynolds and J. H. Ferziger, 1975: Three-dimensional time-dependent computation of turbulent flows. Rep. TF-5, Dept. Mech. Eng., Stanford University.

Lenschow, D. H., J. C. Wyngaard and W. T. Pennell, 1980: Mean-field and second-moment budgets in a baroclinic, convective boundary layer. *J. Atmos. Sci.*, **37,** 1313–1326.

Leonard, A., 1974: Energy cascade in large eddy simulations of turbulent fluid flows. *Advances in Geophysics,* Vol. 18, Academic Press, 237–248.

Lilly, D. K., 1966: On the application of the eddy-viscosity concept in the inertial subrange of turbulence. Manuscript No. 123, National Center for Atmospheric Research, Boulder, CO, 19 pp.

——, 1967: The representation of small-scale turbulence in numerical simulation experiments. *Proc. IBM Scientific Computing Symp. on Environmental Science,* Thomas J. Watson Research Center, Yorktown Heights, 195–210.

Love, M. D., and D. C. Leslie, 1977: Studies of subgrid modeling with classical closures and Burger's equation. *Symp. on Turbulent Shear Flows,* Pennsylvania, 14.1–14.10.

Mansour, N. N., P. Moin, W. C. Reynolds and J. H. Ferziger, 1979: Improved methods for large eddy simulations of turbulence. *Turb. Shear Flows,* **1,** 386–401.

Moeng, C.-H., and D. A. Randall, 1984: Problems in simulations of the stratocumulus-topped boundary layer with a third-order closure model. *J. Atmos. Sci.*, **41,** 1588–1600.

Moin, P., W. C. Reynolds and J. H. Ferziger, 1978: Large eddy simulation of incompressible turbulent channel flow. Rep. No. TF-12, Thermoscience Div., Stanford, CA.

Orszag, S. A., 1971a: Numerical simulation of incompressible flows within simple boundaries: Accuracy. *J. Fluid Mech.*, **49,** 75–112.

——, 1971b: On the elimination of aliasing in finite-difference schemes by filtering high-wavenumber components. *J. Atmos. Sci.*, **28,** 1074.

Reynolds, W. C., 1981: Simulation of turbulent shear flows: What can we do and what have we learned? *Seventh Biennial Symp. on Turbulence,* Rolla, 13.

Schumann, U., G. Grötzbach and L. Kleiser, 1980: Direct numerical simulation of turbulence. *Prediction Methods for Turbulent Flows,* W. Kollman, Ed., Hemisphere, 123–158.

Smagorinsky, J., 1963: General circulation experiments with the primitive equations. *Mon. Wea. Rev.*, **91,** 99–165.

Sommeria, G., 1976: Three-dimensional simulation of turbulent processes in an undisturbed tradewind boundary layer. *J. Atmos. Sci.*, **33,** 216–241.

Taylor, G. I., and A. E. Green, 1937: Mechanism of the production of small eddies from large ones. *Proc. Roy. Soc. London,* **A158,** 499–521.

Wyngaard, J. C., 1973: On surface layer turbulence. *Workshop on Micrometeorology,* Amer. Meteor. Soc., 101–148.

Zeman, O., and J. L. Lumley, 1976: Modeling buoyancy-driven mixed layers. *J. Atmos. Sci.*, **33,** 1974–1988.